Engineering Structures 183 (2019) 150–159

Contents lists available at ScienceDirect

Engineering Structures

journal homepage: www.elsevier.com/locate/engstruct

Post-fire seismic behavior of two-bay two-story frames with high-performance fiber-reinforced cementitious composite joints

Xiuling Li[a], Zhenbo Xu[a], Yi Bao[b,*], Zhengang Cong[a]

[a] School of Civil Engineering, Shandong Jianzhu University, Fengming Road, Jinan, Shandong 250101, China
[b] Department of Civil, Environmental and Ocean Engineering, Stevens Institute of Technology, Hoboken, NJ 07030, United States

ARTICLE INFO

Keywords:
Fire damage
Frame
High-performance fiber-reinforced cementitious composites
Multi-hazard evaluation
Post-fire performance
Seismic behavior

ABSTRACT

High-performance fiber-reinforced cementitious composite (HPFRCC) has potential to greatly improve the fire resistance and seismic behavior of concrete structures. This paper reports an experimental investigation on post-fire seismic behavior of two-bay two-story frames with HPFRCC joints. Four reinforced concrete frames were fabricated; three of them were tested in compartment fire for 60 min. The fire was regulated following ISO-834 temperature curve. Two different fire scenarios (one- and two-bay fire) were investigated. Two frames were made of monotonic conventional concrete; the other two frames had HPFRCC joints. Each frame was tested under a constant vertical load and a pseudo-static cyclic horizontal load with increased magnitude until the frame failed. The effects of the HPFRCC and fire scenarios on the failure mechanism, hysteretic loops, envelope curve, stiffness degradation, and energy dissipation of the frames were evaluated. The experimental results revealed that the fire exposure reduced the load capacity and deformability of the frames. In the two-bay fire scenario, the use of HPFRCC joints increased the post-fire load capacity by 11%, ultimate deformation by 6%, initial stiffness by 30%, and energy dissipation by 21%. The cyclic behavior of the frame in one-bay fire was better than that in two-bay fire. The frames with HPFRCC joints demonstrated better cyclic behaviors than the virgin reinforced concrete frame.

1. Introduction

Fire hazards continue to occur in civil engineering structures such as buildings, tunnels, and bridges, and cause catastrophic consequences. The fire behaviors of beams [1–3], slabs [4–6], and columns [7] and frames [8,9] were investigated through experimentation and/or finite element analysis. Effects of different fire scenarios, fire duration, and structural design variables on the structural degradation were evaluated [1–9]. It is agreed that fire exposure can reduce the load-bearing capacity of civil engineering structures. In a fire hazard, the elevated temperature reduces the mechanical strengths of concrete [10,11] and steel bars [10,12], as well as the bond between concrete and steel bars [13,14]. In addition, the elevated temperature may cause explosive spalling in concrete [15]. Concrete spalling may expose steel bars to fire and thus accelerate the degradation of the structure.

In recent years, different families of high-performance fiber-reinforced cementitious composites (HPFRCCs) have been developed to improve the mechanical performance, resilience and durability of concrete structures [16,17]. Ultra-high-performance concrete (UHPC) is a family of HPFRCC with extreme compressive and tensile strengths, durability and flowability due to the refined microstructure and well-designed chemistry [18–21]. Typically, UHPC has a very low water-to-binder ratio (w/b < 0.25) and uses finely ground silica sand. Most recently, river sand and high-volume supplementary cementitious materials such as fly ash and/or ground granulated blast slag have been used to reduce the materials cost and carbon footprint [16,17]. However, the very dense microstructure makes UHPC susceptible to explosive spalling at elevated temperatures due to continuous buildup of internal vapor pressure [15]. Engineered cementitious composite (ECC) is another representative family of HPFRCC and featured with the very high tensile ductility ($\sim$4%) [21–23]. ECC has improved fire resistance due to the use of polymeric fibers such as polyvinyl alcohol (PVA) fibers, which can melt and create channels to alleviate internal vapor pressure, thus preventing explosive spalling [24–31]. In fire tests of HPFRCC specimens with PVA fibers, no or minor spalling was observed; post-fire mechanical properties were higher than conventional concrete; preferred thermal properties that tended to decelerate heat transfer in HPFRCC were demonstrated [32,33]. Post-fire pull-out tests of steel bars embedded in HPFRCC showed that the use of HPFRCC enhanced the bond strength [34]. Thus, HPFRCC has great promise to

* Corresponding author.
E-mail address: yi.bao@stevens.edu (Y. Bao).

https://doi.org/10.1016/j.engstruct.2019.01.015
Received 4 October 2018; Received in revised form 25 December 2018; Accepted 3 January 2019

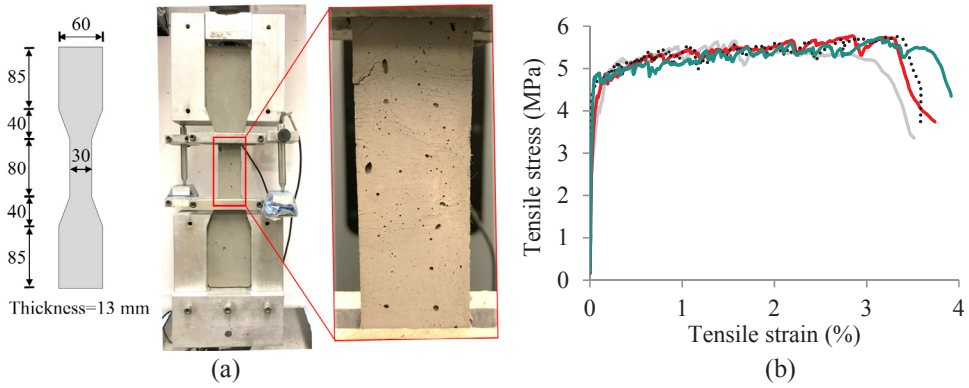

Fig. 1. Tensile test: (a) setup and specimen (unit: mm); (b) stress-strain curves.

improve the performance of structures in fire.

In addition to the promising improvement of fire resistance, HPFRCC has been proven effective in enhancing the seismic behavior of structures [35]. Fibers mixed in the HPFRCC can bridge cracks and thus reduce damages in HPFRCC structures [35–37]. However, to date, there has been no study on the post-fire seismic behavior of reinforced concrete structures with HPFRCC. It remains unknown whether the use of HPFRCC with polymeric fibers can improve the seismic performance of structures after exposure to fire, because the polymeric fibers melt at elevated temperatures. Absence of the polymeric fibers due to fire may significantly compromise the port-fire seismic behavior. Such knowledge gap hinders the designs and engineering applications of HPFRCC in structures.

The primary objective of this research is to investigate the post-fire seismic behavior of reinforced concrete frames through experimentation. To this end, four two-bay two-story frames were fabricated and tested. Three frames were exposed to ISO-834 fire for one hour [38]; the other frame was not exposed to any fire and taken as the control specimen. Among the three frames exposed to fire, two frames had HPFRCC joints. Two fire scenarios (one-bay and two-bay fire) were investigated. The four frames were then tested until failure under constant vertical loading and cyclic horizontal loading.

2. Materials

2.1. Conventional concrete

A conventional concrete with a water-to-cement ratio of 0.46 was used. The maximum size of coarse aggregates was 16 mm. The compressive and splitting tensile strengths of concrete cylinders were determined to be 32 MPa and 1.8 MPa, respectively.

2.2. Steel reinforcement

Two sizes (Φ8 and Φ10) of plain steel bars were used as stirrups, and two sizes (Φ14 and Φ25) of deformed steel bars were used as longitudinal reinforcement, in accordance with GB1499.2-2007 [39]. The nominal diameters of Φ8, Φ10, Φ14 and Φ25 are 8 mm, 10 mm, 14 mm, and 25 mm, respectively. The plain steel bars had yield and ultimate strengths of 300 MPa and 420 MPa, respectively; the deformed steel bars had yield and ultimate strengths of 400 MPa and 540 MPa, respectively. The Young's modulus of the steel bars was 205 GPa.

2.3. HPFRCC mixture

A HPFRCC mixture developed in a previous study [33] was adopted as a structural material in this study. The mixture was prepared using ASTM Type I Portland cement, Class F fly ash, finely ground quartz sand, polyvinyl alcohol (PVA) fibers, and water. The quartz sand has an average diameter of 75 μm, a density of 2.63 g/cm^3, and a SiO_2 content of 98.9%. The PVA fibers were 12 mm in length, 39 μm in diameter, and 1300 kg/m^3 in density; their tensile strength and ultimate elongation were 1.6 GPa and 6–8%, respectively; the elastic modulus and Poisson's ratio were 43 GPa and 0.42, respectively; the melting temperature of the PVA fibers was 225 °C.

The HPFRCC mixture was proportioned with high-volume fly ash to reduce the embodied energy and carbon footprint. A total of 60% of cement was replaced with the fly ash. The w/b was set to 0.24; the sand-to-binder ratio of 0.46; the PVA fiber volume percentage was 2% by the volume of the composite. A polycarboxylic acid based high range water reducer was used at a dosage of 0.1% by volume of the binder to improve the flowability.

The mixture was mixed using a 60-Qt. Hobart mixer. The cement, fly ash, and quartz sand were first mixed in dry condition at 60 rpm for 5 min (min). The high range water reducer was dissolved in water, and then introduced to the mixer and mixed at 120 rpm for 5 min. Finally, the PVA fibers were added by hand at 60 rpm within 2 min, followed by mixing at 120 rpm for 3 min. On completion of mixing, the mixture was checked by hand, and no fiber agglomeration was found.

Five cubic specimens with a 150 mm side length were tested under compression at 28 days in accordance with JGJ/T70-2009 [40]. The compressive strength was 40 MPa ± 2 MPa. Four dog-bone specimens (Fig. 1(a)) were tested under tension at a displacement rate of 0.05 mm/min in accordance with [41]. The applied load and specimen elongation within the 80 mm gauge length were measured using an embedded load cell and two external linear variable differential transformers (LVDTs), respectively. Fig. 1(b) shows a set of tensile stress–strain curves. The mixtures had a tensile strength of 5.3 MPa ± 0.3 MPa and an ultimate strain of 3.2% ± 0.4%.

3. Experimental program

3.1. Specimens

Four two-bay two-story frames were designed to represent typical reinforced concrete frames of buildings in accordance with GB50010-2010 [42]. In each frame, for seismic considerations, the columns were designed to be stronger than the beams; the joints were stronger than the columns and beams. The four frames, designated as S-1 to S-4, had the same reinforcement and dimensions. Fig. 2(a) and (b) depict the frames; Fig. 2(c) illustrates the reinforcement details. The concrete cover thickness was 20 mm. Each frame measured 3280 mm in height and 3400 mm in width, and was cast on an I-shaped footing. Each beam had a 200 mm × 160 mm rectangular cross section reinforced with four Φ14 bars along the beam. Each column had a 200 mm × 200 mm square cross section reinforced with eight Φ14 bars along the column. The beams and columns were reinforced using Φ8 stirrups spaced at 100 mm, except for the beam/column joints (Fig. 2(b)), where the

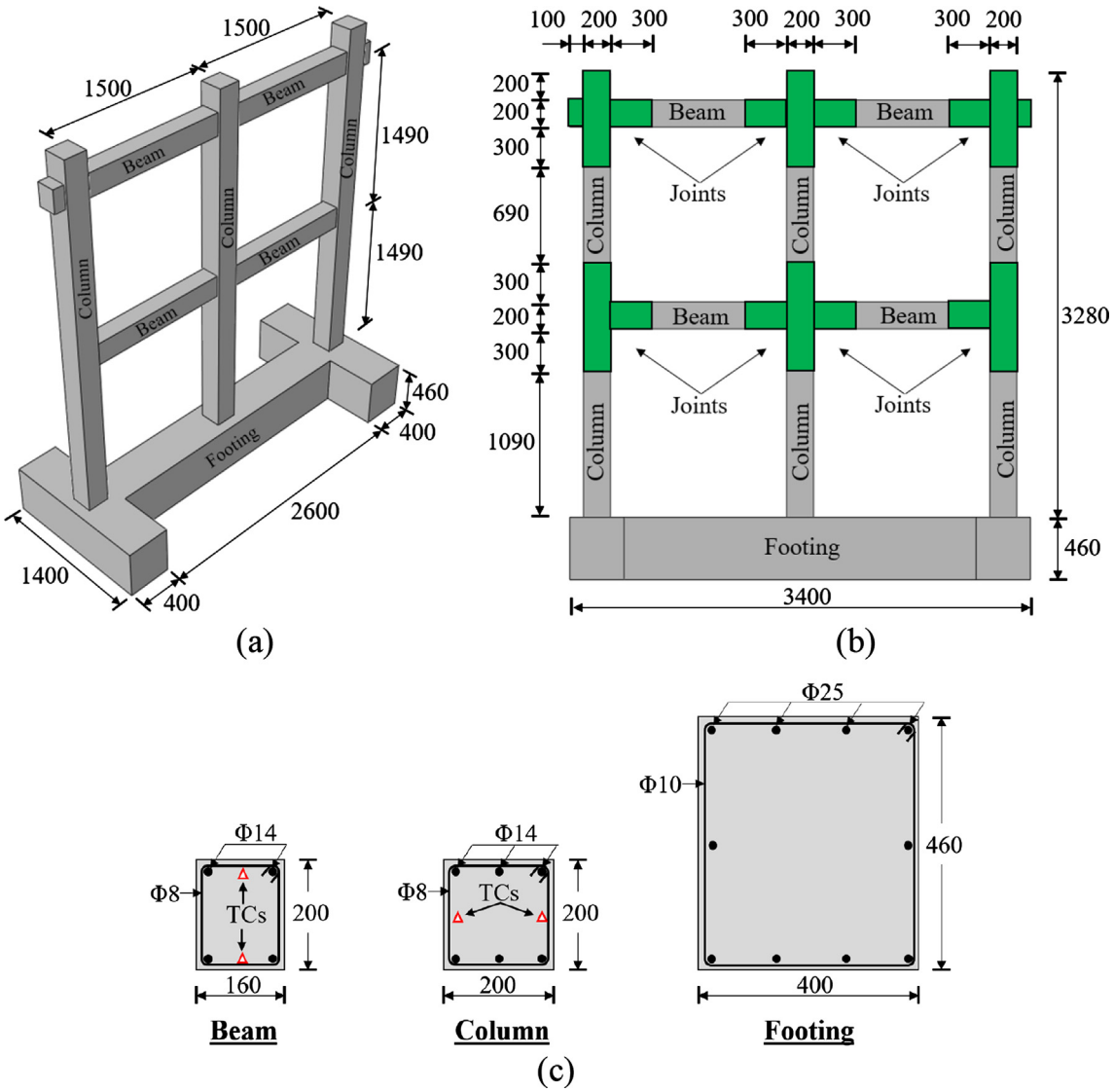

Fig. 2. Dimension and reinforcement of frame specimens (unit: mm): (a) perspective view; (b) elevation view; (c) reinforcement in cross sections.

spacing of stirrups was down to 50 mm. The footing had a 460 mm × 400 mm rectangular cross section reinforced with eight Φ25 bars and Φ10 stirrups spaced at 100 mm. The cross section of the footing was designed to achieve load-carrying capacity and flexural stiffness much larger than those of the columns. Thus, the footing can be considered as rigid compared with the columns.

Fig. 3 illustrates the four frames. S-1 was not exposed to any fire and taken as the control specimen; S-2, S-3, and S-4 were exposed to fire: S-2 and S-3 were subjected to fire at two bays, while S-4 was only subjected to fire at one bay. S-1 and S-2 were made of monotonic conventional concrete; the joints of S-3 and S-4 were made using the HPFRCC. For the fabrication of the joints in S-3 and S-4, an acrylic plate measuring 3.2 mm in thickness was placed at the interface between fresh concrete and HPFRCC during casting, and then removed immediately after casting. A concrete vibrator was used to consolidate each interface zone to ensure an adequate wet joint. The specimens were cured in air for 28 days before fire testing.

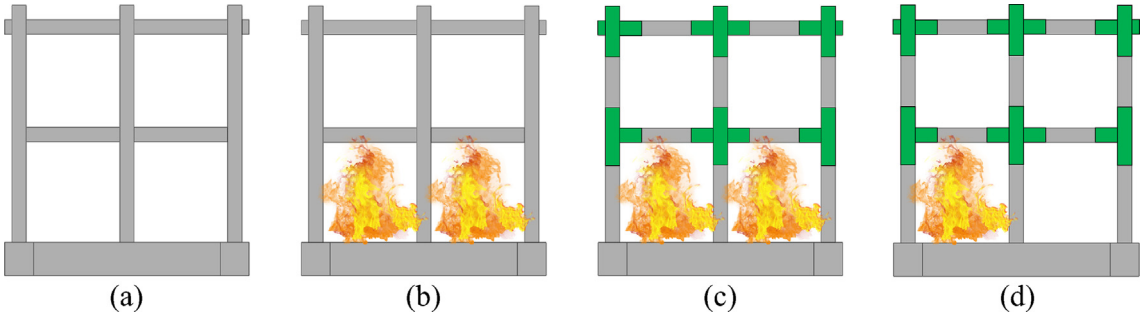

Fig. 3. Illustration of the specimens: (a) S-1; (b) S-2; (c) S-3; (d) S-4.

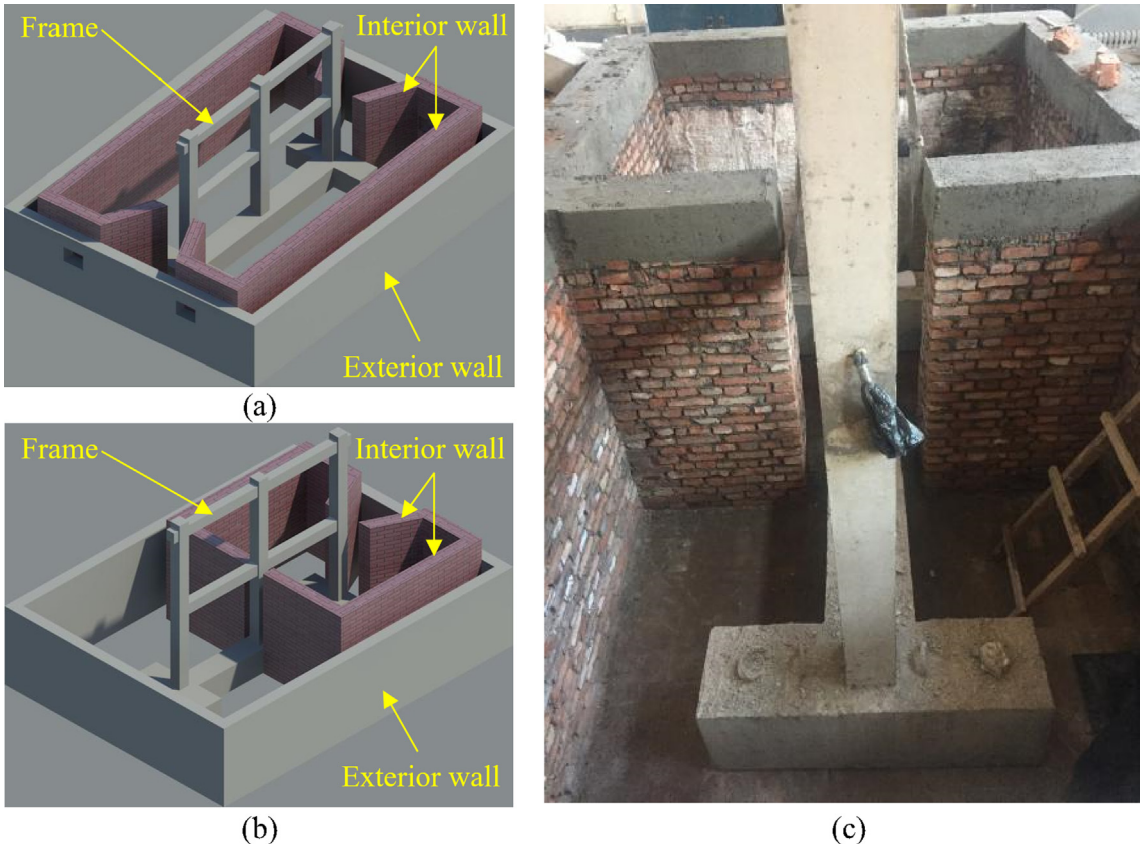

Fig. 4. Furnace for fire test: (a) illustration of furnace for two-bay fire test; (b) illustration of furnace for one-bay fire test; (c) photograph of frame in compartment for the one-bay fire test.

3.2. Furnace and fire exposure

A customized furnace was built for the compartment fire test, as depicted in Fig. 4(a)–(c). In the furnace, the interior walls were built using fire-proofing masonry bricks for the different fire scenarios, as illustrated in Fig. 4(a) and (b). The interior walls served as thermal insulation for the other parts of the frame outside of the interior walls. The exterior walls were built with reinforced concrete for safety considerations of the laboratory. The furnace was covered using four reinforced concrete slabs on the top. Each of the four slabs was 100 mm in thickness. The interior walls, cover slabs, and footing of the frame were protected using high-temperature proofing wool with a very low thermal conductivity for thermal insulation.

The frames S-2, S-3, and S-4 were exposed to the ISO-834 standard fire [38]. The fire magnitude was regulated through controlling the heat release rate of the burner, the same as the method specified in [2,3]. A glass-sheathed, bare bead, K-type thermocouple was deployed 25 mm below the cover slabs at the center of the compartment for measuring the upper-layer gas temperature. The thermocouple had a ceramic coating for protection from high temperature and moisture in concrete. The thermocouples have a manufacturer-specified temperature standard limit of error of 2.2 °C or 0.75% (whichever value is greater) over a measurement range of 0 °C to 1250 °C. Data from the thermocouples were recorded using a data acquisition system at a sampling frequency of 10 Hz. Fig. 5 plots the ISO-834 temperature curve (only the ascending part) and the measured gas temperature (both the ascending and the descending parts).

3.3. Test setup, instrumentation, and loading protocol

Each frame was tested under a constant vertical load and horizontal cyclic load with an incrementally increasing magnitude. Fig. 6

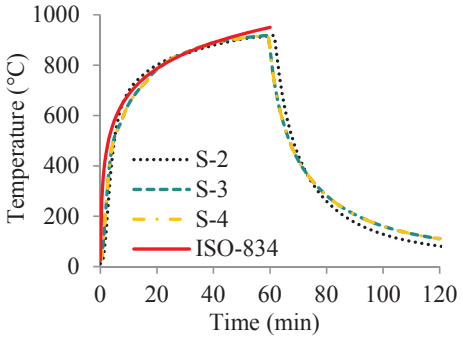

Fig. 5. Temperature-time curves for the fire tests of the three frames (S-2, S-3 and S-4).

illustrates the test setup. The footing of the test frame was anchored to the strong floor of the laboratory with steel bolts measuring 50 mm in diameter. Each specimen was loaded using two 1000-kN load actuators with a stroke distance of ± 250 mm in the vertical and horizontal directions. In the vertical direction, the load was applied to the three columns of the frame through rigid steel beams that served as spreaders. The distances between the rollers and supports were designed to apply equal vertical loads on the three columns; for each span, the load to support distance ratio was 1:2 (see Fig. 6). The vertical load of each column was monitored using a load cell with a capacity of 500 kN and a measurement accuracy of 50 N. An axial load of 255 kN was applied to each column and kept constant throughout the test. The applied vertical load corresponded to approximately 15% of the axial load-bearing capacity of each column and represented the effect of gravity loads of supported upper floors [35]. The horizontal actuator was pin-supported on an L-shape reaction wall at one end and connected to the load stub of

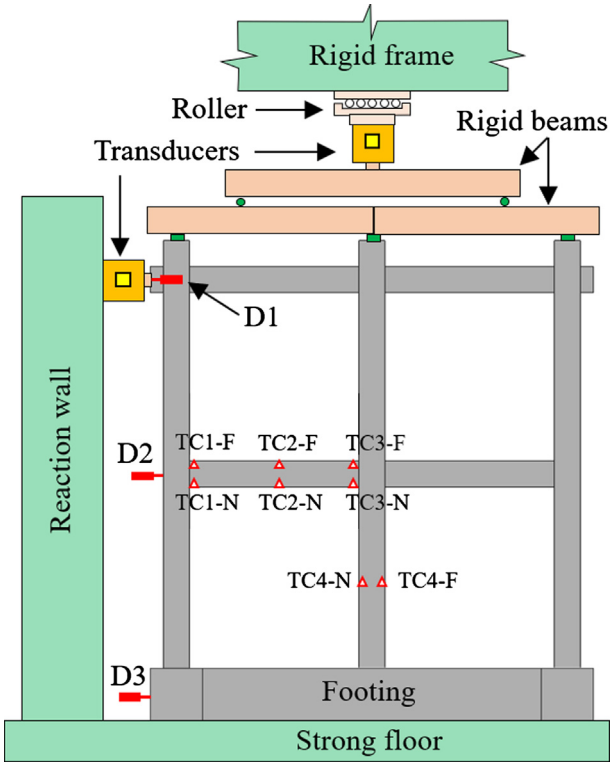

Fig. 6. Experimental setup for cyclic loading test. D1 to D3 are displacement sensors. TC represents the K-type thermocouple.

the top beam at the other end to apply a lateral load to the frame.

Three LVDTs were used for measuring displacement of the frame. Each of the LVDTs had a measurement range of ± 100 mm and an accuracy of 0.02 mm. The three LVDTs were designated as D1, D2 and D3. Among them, D1 and D2 measured the horizontal displacements of the beams at the two stories; D3 measured the horizontal displacement of the footing. In S-1, S-3 and S-4, eight thermocouples (TCs) that were designated from TC1 to TC4 at four cross sections were used to measure temperature in the frame, as shown in Figs. 2(c) and 6. At each of the four cross sections, two thermocouples are respectively deployed at the near (N) and far (F) fire sides. For instance, TC1-N represents the thermocouple at the near fire side of section for TC1.

Each frame was subjected to an amplitude-increasing loading under displacement control [28], as illustrated in Fig. 7. The amplitude of loading cycles was increased by 2 mm every two cycles. Each amplitude

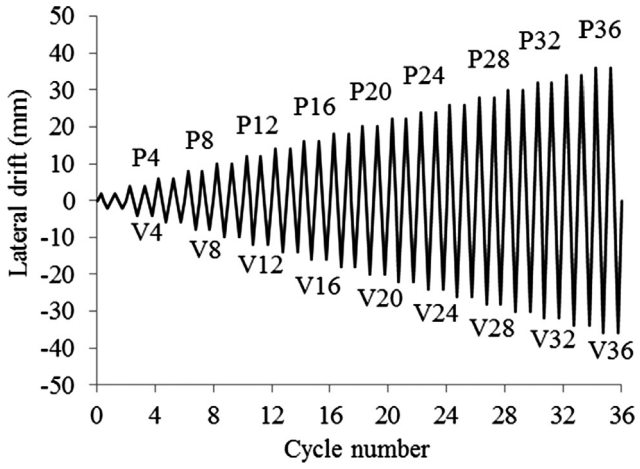

Fig. 7. The frames were tested under amplitude-increasing cyclic loading.

was repeated in two cycles to show cyclic deterioration without causing potential fatigue damage of the steel bars. The peaks (maximum) in ascending order were designated as P1, P2, P3, ⋯, and P36. Correspondingly, the valleys (minimum) were designated as V1, V2, V3, ⋯, and V36. The test was terminated when the load applied on the specimen was reduced to 85% of the load capacity of the column.

4. Test results and discussions

4.1. Visual inspection

In the fire test, after fire ignition for about 10 min, spalling sound was heard in the test of S-2. After that, spalling was heard every 2–5 min. After testing, severe spalling was observed on the columns, beams and joints in S-2, as shown in Fig. 8(a). The spalling was due to two mechanisms. As temperature increases, vapor pressure in the concrete matrix increases due to water vaporization and decomposition of cement hydrates [25,26]; at the same time, thermal degradation of concrete occurs, reducing the mechanical strength of concrete [27–29]. Similar phenomenon of spalling was observed on the surfaces of beams and columns in S-3 and S-4. However, no spalling was observed on the HPFRCC joints, as shown in Fig. 8(b). This is because (1) the PVA fibers in the HPFRCC melt at elevated temperatures and create channels to release vapor pressure in the HPFRCC [33]; and (2) the PVA fibers reduce the thermal conductivity coefficient and delay the temperature increase in the HPFRCC [33].

Fig. 9(a)–(d) shows the failure modes of the frames under cyclic loading. Fig. 9(a) and (b) shows significant concrete cracking and spalling at the joints, ends of the beams, and bottom of the columns in S-1 and S-2. At the joints, the cracks had an inclination angle of about 40° to 50°. S-1 and S-2 had limited number of cracks, and the crack width was up to about 10 mm. The crack spacing was about 50–100 mm. S-1 and S-2 had similar damage patterns, indicating that the fire exposure did not affect the damage pattern of the reinforced concrete frame. However, Fig. 9(c) and (d) shows that the HPFRCC joints not exposed to fire had densely-distributed fine cracks. The crack width was at the order of 1 mm, and the crack spacing was about 10 mm or less. For the HPFRCC joints exposed to fire, the crack width was about 1–5 mm, and the crack spacing was about 20–50 mm. The PVA fibers could not be observed in the HPFRCC near the concrete surface, but the fibers were observed inside of the HPFRCC. Except minor surface flakes, no severe concrete spalling was observed at the HPFRCC joints.

4.2. Temperature

Fig. 10 shows the temperature histories measured from the thermocouples in the S-3 tested in the two-bay fire scenario. TC4-F failed before the fire testing. At the four cross sections, the temperature increases with time due to heat transfer through the concrete and HPFRCC; the temperature at the near fire side is higher than that at the far fire side. At 60 min before fire extinguishment, the measured maximum temperature is up to 610 °C; the minimum temperature is only about 100 °C. At the same cross section, the temperature difference is about 450 °C between the near and far fire sides. Temperature measurement results help explain the visual observation of PVA fibers in the HPFRCC. At the near fire end of frames exposed to fire, PVA fibers melted because the temperature was much higher than the melting point (225 °C) of the fibers. However, PVA fibers were left in the HPFRCC where the temperature did not exceed the melting point throughout the fire test.

4.3. Hysteresis behavior

The loads applied through the horizontal actuator on each frame are plotted in Fig. 11(a)–(e) as a function of the horizontal drift (D1-D3)

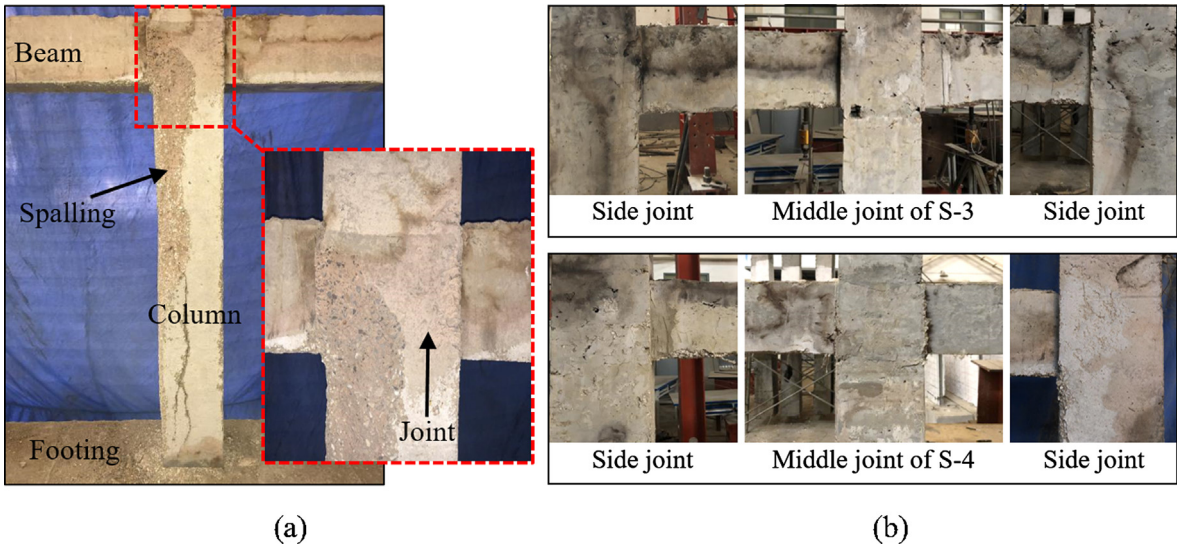

Fig. 8. Photography of damaged specimens: (a) S-2 exhibits severe explosive spalling in fire; (b) S-3 and S-4 do not have spalling at the HPFRCC joints.

(see Fig. 6). The positive and negative loads (and displacements) correspond to the two directions when the actuator pushes and pulls the frame in reference to the reaction wall (see Fig. 6). The load-displacement curves show hysteresis loops with slightly different behaviors in the two directions due to accumulative damage in the frames. In comparison with S-3 and S-4 with HPFRCC joints, S-1 and S-2 demonstrate more severe pinch effect in the hysteretic loops, as shown in Fig. 11(a)–(d). This is because of the unique post-crack behavior of HPFRCC (see Fig. 1). After cracks are produced in the matrix of HPFRCC, due to the presence of PVA fibers that bridge the cracks, the HPFRCC can resist higher tensile force, similar to steel in this sense. In addition, the average crack opening width is typically limited to less than 0.1 mm [20–23]. Therefore, the pinch effect is alleviated by using the HPFRCC at the joints.

As shown in Fig. 11(a) in the positive direction, S-1 reached the ultimate load of $F_u = 114$ kN at a displacement of $D = 96$ mm and the ultimate displacement of $D_u = 164$ mm at 85% of the ultimate load. In the negative direction, the specimen reached the ultimate load of $F_u = 105$ kN at a displacement of $D = 106$ mm and the ultimate displacement of $D_u = 164$ mm. The characteristic load and displacement for all tested frames are summarized in Table 1.

4.4. Load capacity and displacement ductility

Fig. 12(a) compares envelope curves of the hysteresis loops of the frames as presented in Fig. 11. For each frame, the applied load linearly increased with the displacement till the onset of cracking, and then nonlinearly increased at reduced stiffness due to accumulative damage in the column at large displacements. The larger of the two ultimate loads, F_u in Table 1 in positive and negative directions, represents the load capacity of the column. The ultimate displacement, D_u in Table 1, corresponds to the load that drops to 85% of the peak load. Fig. 12(b) compares the experimental results of load capacity and ultimate displacement of the frames. The load capacity of S-2 is 6% lower than that of S-1; the ultimate displacement of S-2 is 7% larger than that of S-1, indicating that exposure to fire slightly reduced the load capacity but increased the ultimate displacement of the frame. The decrease of load capacity and increase of deformability of the frame are associated with the thermal degradation of concrete after exposure to high temperature [10,32]. The residual compressive strengths of concrete [10] and HPFRCC [32] decrease with the heating temperature; the residual deformability of concrete and HPFRCC increase with the heat temperature. In comparison with S-2, the load capacity and ultimate displacement of S-3 are 6% and 3% higher, respectively, revealing that the use of HPFRCC at the joints improved the post-fire load capacity and deformability. The load capacity and ultimate displacement of S-4 are respectively 19% and 21% higher than those of S-3. This is because S-4 was exposed to one-bay fire and thus had a smaller fire exposure area than that of S-3. It should be noted that S-3 and S-4 had higher load capacity and larger ultimate deformation that those of S-1, which was not exposed to any fire, suggesting that post-fire load capacity and deformability of the frame with HPFRCC joints are higher than that of virgin reinforcement concrete frame.

4.5. Stiffness degradation

With the onset and propagation of cracks, the lateral stiffness of the test frame was reduced with increasing lateral displacement. In this study, secant stiffness was used to represent the overall stiffness of the frame. For any loading cycle, the secant stiffness K_i can be expressed as:

$$K_i = \frac{|+F_i| + |-F_i|}{|+X_i| + |-X_i|} \quad (1)$$

where X_i is the peak displacement in the ith cycle of a displacement-control loading protocol and F_i is the corresponding peak load in the ith cycle.

Fig. 13 compares the stiffness of the frames. For each frame, the stiffness degrades as the horizontal displacement increases, due to presence of cracks and spalling in the concrete under cyclic loading. The initial stiffness of S-2 is about 35% lower than that of S-1, indicating that the fire significantly reduced the stiffness of the frame, likely due to the degradation of the mechanical properties and integration of concrete at elevated temperatures [10]. The initial stiffness of S-3 is 30% larger than that of S-2, indicating that the use of HPFRCC at the joints significantly improved the post-fire stiffness of the frame, likely due to the improvement of the mechanical properties and integration of the joints in fire [30]. The initial stiffness of S-4 is 10% higher than that of S-3, indicating that less degradation was caused in the one-bay fire scenario (S-4) than the two-bay fire scenario (S-3), likely due to the reduced area exposed to fire. Another observation is that S-3 and S-4 had comparable initial stiffness with S-1 that was not exposed to any fire, suggesting that the use of HPFRCC at the joints enables the frame to have post-fire stiffness that is comparable with that of virgin reinforced concrete frame. It is noted that the stiffness of S-1 becomes lower than that of S-4 from the second load cycle until the completion of the cyclic loading test. This is because the PVA fibers in

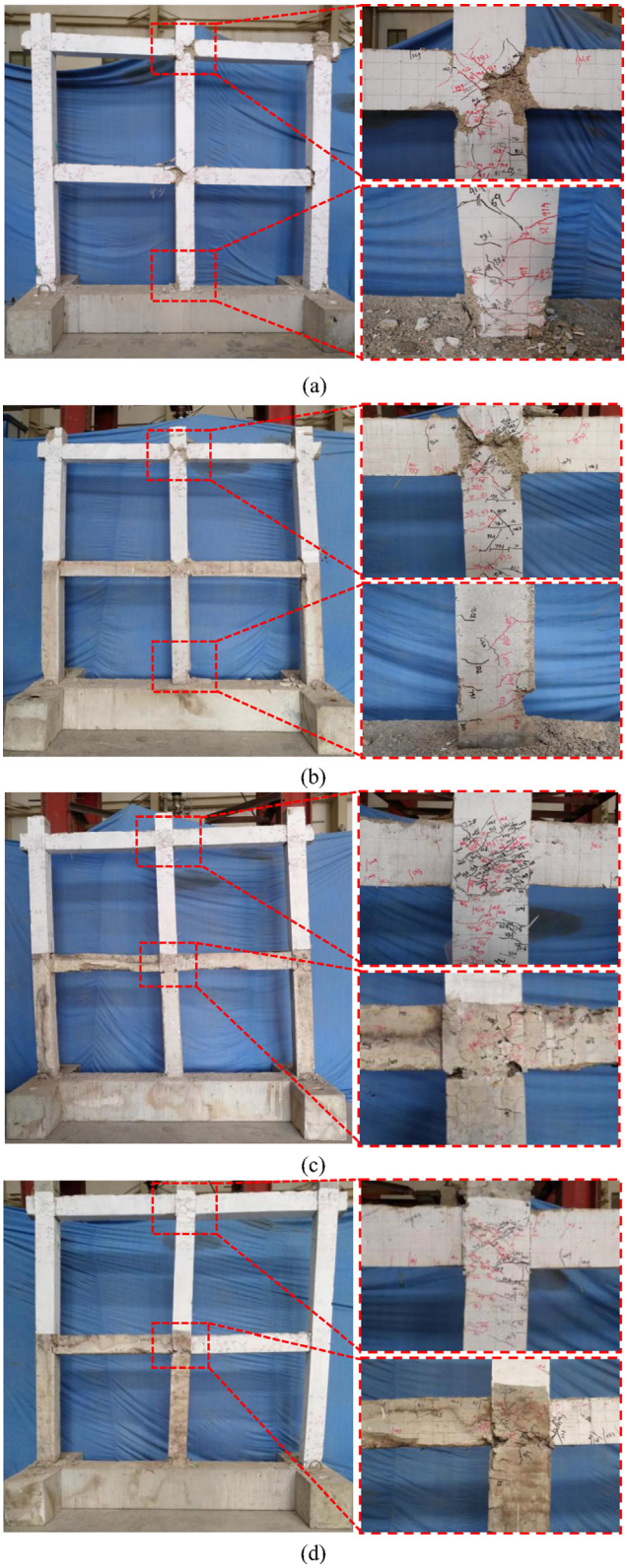

Fig. 9. Photography of specimens tested under cyclic loading: (a) S-1; (b) S-2; (c) S-3; (d) S-4.

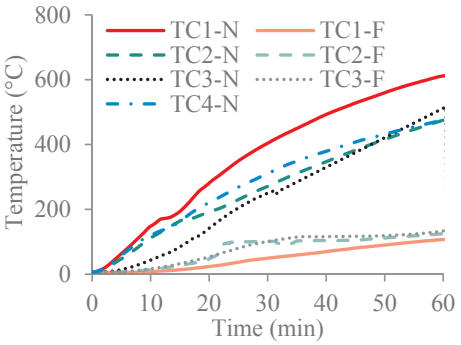

Fig. 10. Temperature histories measured by thermocouples in S-3.

HPFRCC can bridge cracks and thus delay the degradation of stiffness under cyclic loading [35].

4.6. Energy dissipation

The areas enclosed by the load-displacement hysteresis loops represent the energy dissipated during various cycles of loading. In general, larger energy dissipation implies better cyclic performance of columns under seismic loads. In this study, an equivalent viscous damping ratio (h_e) is used to represent the energy dissipation capability [35]. The equivalent viscous damping ratio is defined in Eq. (2):

$$h_e = \frac{S_{ABC} + S_{ADC}}{2\pi (S_{OBE} + S_{ODF})} \quad (2)$$

where S_{ABC}, S_{ADC}, S_{OBE}, and S_{ODF} respectively denote the areas of the triangles of ABC, ADC, OBE, and ODF in the hysteresis curves, as depicted in Fig. 14(a).

The experimental results of the equivalent viscous damping ratios of the frames are compared in Fig. 14(b). Compared with S-1, the equivalent viscous damping ratio of S-2 is reduced by about 10%, indicating that the two-bay fire can compromise the energy dissipation capacity. The equivalent viscous damping ratio of S-3 is 21% higher than that of S-2, indicating that the use of HPFRCC at the joints can improve the energy dissipation capacity. Once again, this is because the use of HPFRCC at the joints can improve the fire resistance and post-fire mechanical properties of the joints where plastic hinges formed and led to failure of the frames in the cyclic loading test. The equivalent viscous damping ratio of S-4 is 11% higher than that of S-3, because S-4 was exposed to fire at a smaller area compared with S-3.

5. Conclusions

Based on the above investigation, the conclusions can be summarized:

- The use of HPFRCC at the joints of the frames protected the integration of the joints. After exposure to ISO-834 fire for one hour, while severe explosive spalling was observed on the conventional concrete, only minor surface flakes were observed at the HPFRCC joints, but no severe explosive spalling was observed on the HPFRCC.
- After the post-fire cyclic testing, the monotonic reinforced concrete frames had limited number of cracks at the joints where plastic hinges formed; the crack width was up to about 10 mm; the crack spacing was about 50 mm to 100 mm. The HPFRCC joints not exposed to fire had densely-distributed fine cracks. The crack width was at the order of 1 mm, and the crack spacing was about 10 mm or less. For the HPFRCC joints exposed to fire, the crack width was about 1 mm to 5 mm, and the crack spacing was about 20 mm to 50 mm.
- For the monotonic reinforced concrete frames, the fire exposure

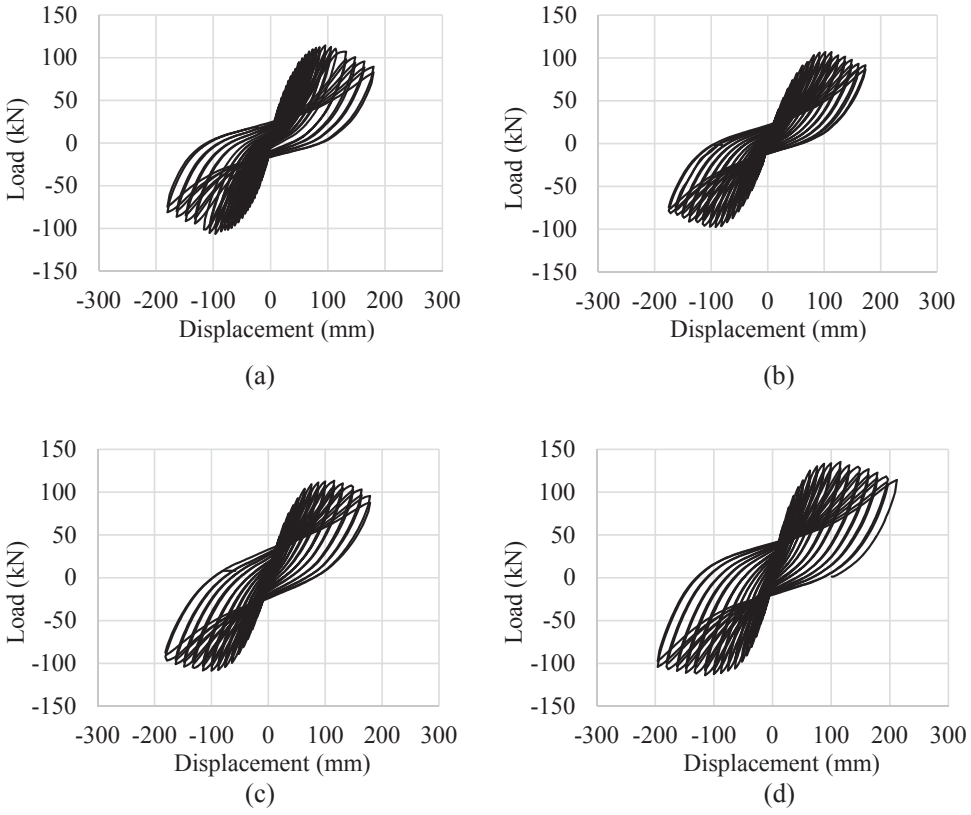

Fig. 11. Hysteretic loops of the frames: (a) S-1; (b) S-2; (c) S-3; (d) S-4.

Table 1
Summary of characteristic load and displacement.

Frame	Positive direction		Negative direction	
	F_u (kN) @ D (mm)	D_u (mm)	F_u (kN) @ D (mm)	D_u (mm)
S-1	114 @ 96	164	105 @ 106	164
S-2	107 @ 102	176	98 @ 92	172
S-3	113 @ 116	180	108 @ 100	182
S-4	135 @ 116	212	114 @ 116	220

reduced the load capacity by 6% and increased the ultimate displacement by 7%. The use of HPFRCC at the joints increased the load capacity and ultimate displacement by 6% and 3%, respectively. The frame with HPFRCC joints subjected to one-bay fire had a load capacity and ultimate displacement that were respectively 19%

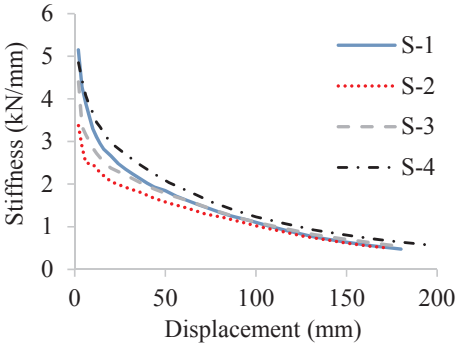

Fig. 13. Stiffness degradation.

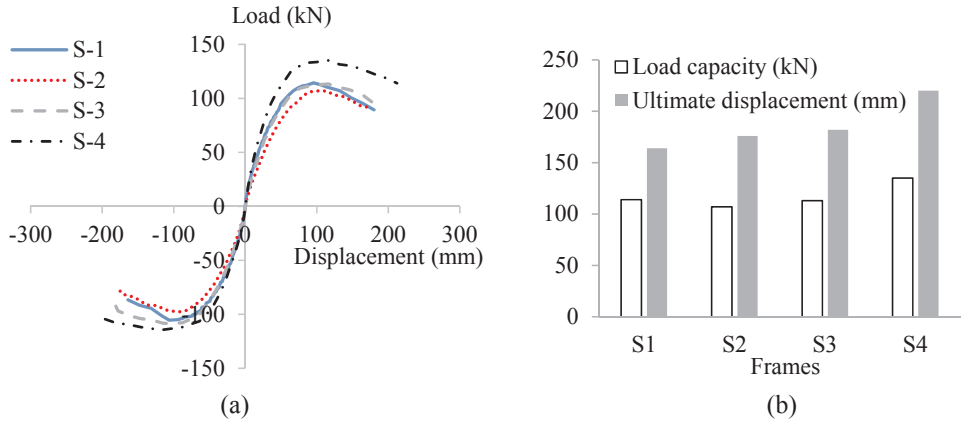

Fig. 12. Load capacity and ductility of the four frames: (a) envelope curves; (b) comparison of the load capacity and ultimate displacement.

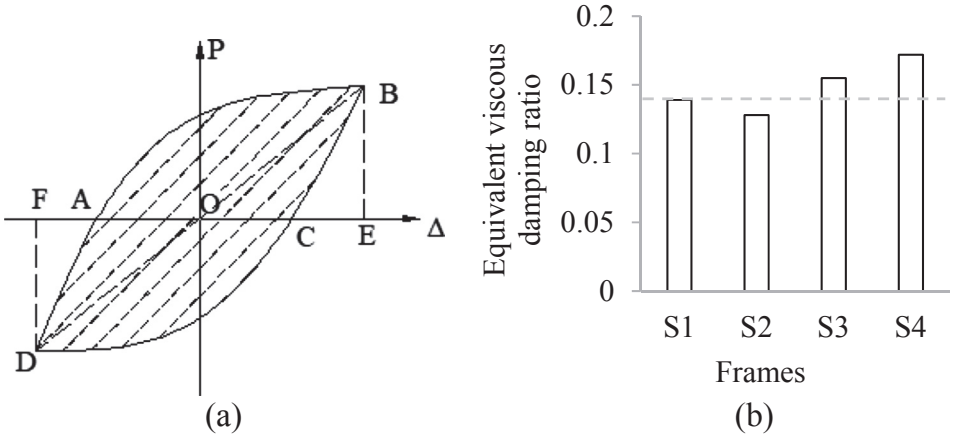

Fig. 14. Dissipated energy: (a) illustration for equivalent viscous damping ratio; (b) experimental results of equivalent viscous damping ratio.

and 21% higher than those of the frame with HPFRCC joints subjected to two-bay fire.

- For the monotonic reinforced concrete frames, the fire exposure reduced the initial stiffness by 35%. The use of HPFRCC at the joints increased the initial stiffness by 30%. Compared with the two-bay fire, the frame subjected to the one-bay fire had an initial stiffness that was 10% higher.
- For the monotonic reinforced concrete frames, the fire exposure reduced the energy dissipation by 10%. The use of HPFRCC at the joints increased the energy dissipation by 21%. In comparison with the frame subjected to the two-bay fire, the frame with HPFRCC joints subjected to the one-bay fire had an energy dissipation capacity that was 11% higher.

Acknowledgements

This study was supported by the Natural Science Foundation of China [grant numbers 51278290 and 51108253]; the Educational Commission of Shandong Province [grant number J11LE09]; the Ministry of Education Innovation Team [grant number IRT13075].

References

[1] Kodur VKR, Agrawal A. Effect of temperature induced bond degradation on fire response of reinforced concrete beams. Eng Struct 2017;142:98–109.
[2] Bao Y, Chen Y, Matthew H, Smith C, Matthew B, Chen G. Experimental analysis of steel beams subjected to fire conditions enhanced by Brillouin scattering based fiber optic sensor data. J Struct Eng 2017;143(1):04016143.
[3] Bao Y, Hoehler MS, Smith CM, Bundy M, Chen G. Temperature measurement and damage detection in concrete beams exposed to fire using PPP-BOTDA based fiber optic sensors. Smart Mater Struct 2017;26(10):105034.
[4] Hawileh RA, Kodur VKR. Performance of reinforced concrete slabs under hydrocarbon fire exposure. Tunn Undergr Space Technol 2018;77:177–87.
[5] Wang Y, Bisby LA, Wang T, Yuan G, Baharudin E. Fire behaviour of reinforced concrete slabs under combined biaxial in-plane and out-of-plane loads. Fire Saf J 2018;96:27–45.
[6] Wang Y, Yuan G, Huang Z, Lyv J, Li ZQ, Wang TY. Experimental study on the fire behaviour of reinforced concrete slabs under combined uni-axial in-plane and out-of-plane loads. Eng Struct 2016;128:316–32.
[7] Zhou K, Han L. Experimental performance of concrete-encased CFST columns subjected to full-range fire including heating and cooling. Eng Struct 2018;165:331–48.
[8] Kamath P, Sharma UK, Kumar V, Bhargava P, Usmani A, Singh B, et al. Full-scale fire test on an earthquake-damaged reinforced concrete frame. Fire Saf J 2015;73:1–19.
[9] Dwaikat M, Kodur V, Quiel S, Garlock M. Experimental behavior of steel beam-columns subjected to fire-induced thermal gradients. J Constr Steel Res 2011;67(1):30–8.
[10] ECS. Eurocode 2: design of concrete structures – Part 1-2: general rules – structural fire design. EN 1992-1-2. European Committee for Standardization; 2004.
[11] Novak J, Kohoutkova A. Mechanical properties of concrete composites subject to elevated temperature. Fire Saf J 2018;95:66–76.
[12] Gardner L, Bu Y, Francis P, Baddoo NR, Cashell KA, McCann F. Elevated temperature material properties of stainless steel reinforcing bar. Constr Build Mater 2016;114:977–97.
[13] Bingöl AF, Gül R. Residual bond strength between steel bars and concrete after elevated temperatures. Fire Saf J 2009;44(6):854–9.
[14] Pothisiri T, Panedpojaman P. Modeling of bonding between steel rebar and concrete at elevated temperatures. Constr Build Mater 2012;27(1):130–40.
[15] Way RT, Wille K. Effect of heat-induced chemical degradation on the residual mechanical properties of ultrahigh-performance fiber-reinforced concrete. J Mater Civ Eng 2015:04015164.
[16] Meng W, Valipour M, Khayat KH. Optimization and performance of cost-effective ultra-high performance concrete. Mater Struct 2017;50(1):29.
[17] Meng W, Khayat KH. Effects of saturated lightweight sand content on key characteristics of ultra-high-performance concrete. Cem Concr Res 2017;101:46–54.
[18] Meng W, Samaranayake VA, Khayat KH. Factorial design and optimization of UHPC with lightweight sand. ACI Mater J 2018;115(1):129–38.
[19] Meng W, Khayat KH. Mechanical properties of ultra-high-performance concrete enhanced with graphite nanoplatelets and carbon nanofibers. Compos B Eng 2016;107:113–22.
[20] Meng W, Lunkad P, Kumar A, Khayat KH. Influence of silica fume and polycarboxylate ether dispersant on hydration mechanisms of cement. J Phys Chem C 2016;120(47):26814–23.
[21] Meng W, Yao Y, Mobasher B, Khayat KH. Effects of loading rate and notch-to-depth ratio of notched beams on flexural performance of ultra-high-performance concrete. Cem Concr Compos 2017;83:349–59.
[22] Li VC, Wang S, Wu C. Tensile strain-hardening behavior of polyvinyl alcohol engineered cementitious composite (PVA-ECC). ACI Mater J 2001;98(6):483–92.
[23] Fischer G, Li VC. Deformation behavior of fiber-reinforced polymer reinforced engineered cementitious composite (ECC) flexural members under reversed cyclic loading conditions. ACI Struct J 2003;100(1):25–35.
[24] Kanda T, Lin Z, Li VC. Tensile stress-strain modeling of pseudo strain-hardening cementitious composites. J Mater Civ Eng 2000;12(2):147–56.
[25] Şahmaran M, Özbay E, Yücel HE, Lachemi M, Li VC. Assessing mechanical properties and microstructure of fire-damaged engineered cementitious composites. ACI Mater J 2010;107(3):297–304.
[26] Bhat PS, Chang V, Li M. Effect of elevated temperature on strain-hardening engineered cementitious composites. Constr Build Mater 2014;69:370–80.
[27] Yu K, Lu Z, Yu J. Residual compressive properties of strain-hardening cementitious composite with different curing ages exposed to high temperature. Constr Build Mater 2015;98:146–55.
[28] Yu K, Dai J, Lu Z, Leung CKY. Mechanical properties of engineered cementitious composites subjected to elevated temperatures. J Mater Civ Eng 2015;27(10):04014268.
[29] Liu J, Tan K. Fire resistance of strain hardening cementitious composite with hybrid PVA and steel fibers. Constr Build Mater 2017;135:600–11.
[30] Liu J, Tan K. Fire resistance of ultra-high performance strain hardening cementitious composite: Residual mechanical properties and spalling resistance. Cem Concr Compos 2018;89:62–75.
[31] Liu J, Tan K, Yao Y. A new perspective on nature of fire-induced spalling in concrete. Constr Build Mater 2018;184:581–90.
[32] Li X, Xu H, Meng W, Bao Y. Tri-axial compressive properties of high-performance fiber-reinforced cementitious composites after exposure to high temperatures. Constr Build Mater 2018;190:939–47.
[33] Li X, Bao Y, Wu L, Yan Q, Ma H, Chen G, et al. Thermal and mechanical properties of high-performance fiber-reinforced cementitious composites after exposure to high temperatures. Constr Build Mater 2017;157:829–38.
[34] Li X, Bao Y, Xue N, Chen G. Bond strength of steel bars embedded in high-performance fiber-reinforced cementitious composite before and after exposure to elevated temperatures. Fire Saf J 2017;92:98–106.
[35] Li X, Wang J, Bao Y, Chen G. Cyclic responses of reinforced concrete columns retrofitted using a green high-performance fiber-reinforced cementitious composite. Eng Struct 2017;136:26–35.
[36] Meng W, Khayat KH. Experimental and numerical studies on flexural behavior of ultra-high performance concrete panels reinforced with embedded glass fiber-reinforced polymer grids. Transp Res Rec: J Transp Res Board 2016;2592:38–44.

[37] Meng W, Khayat KH. Improving flexural behavior of ultra-high performance concrete by rheology control. Compos B Eng 2017;117:26–34.
[38] ISO 834-10:2014. Fire resistance tests – elements of building construction – Part 10: specific requirements to determine the contribution of applied fire protection materials to structural steel elements.
[39] Ministry of Construction of the People's Republic of China. GB1499.2-2007. Steel for the reinforcement of concrete. Part 2: Hot rolled ribbed bars. Beijing: China Architecture Industry Press; 2007.
[40] Ministry of Construction of the People's Republic of China. JGJ/T70-2009. Standard for test method of performance on building mortar. Beijing: China Architecture Industry Press; 2009.
[41] Japanese Society of Civil Engineers (JSCE). Recommendations for Design and Construction of High Performance Fiber Reinforced Cement Composites with Multiple Fine Cracks (HPFRCC); 2008, Japan.
[42] Ministry of Construction of the People's Republic of China. GB50010-2010. Code for design of concrete structures. Beijing: China Architecture Industry Press; 2010.